Electronic Journal of Biotechnology 64 (2023) 42–58

Contents lists available at ScienceDirect

Electronic Journal of Biotechnology

journal homepage: www.elsevier.com/locate/ejbt

Research Article

Prognostic implication of a ferroptosis-related gene signature associates with immunity in Ewing's sarcoma

Xiejia Jiao [a], Qingbo Li [a,*], Xiao Xu [b]

[a] Department of Orthopedic, Second Hospital of Shandong University, Jinan, China
[b] Sterile Supply Department, The First People Hospital of Jinan, Jinan, China

GRAPHICAL ABSTRACT

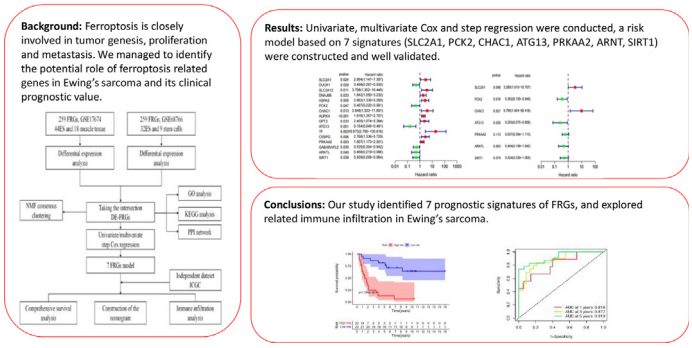

ARTICLE INFO

Article history:
Received 8 October 2022
Accepted 23 January 2023
Available online 28 April 2023

Keywords:
Bone sarcoma
Cancer
Ewing's sarcoma
Ferroptosis
FRGs
Immune
Nomogram
Prognosis
Risk model
Signatures
Survival

ABSTRACT

Background: Ewing's sarcoma is an extremely aggressive bone sarcoma in teenagers and adolescents. We managed to identify the potential role of ferroptosis-related genes (FRGs) in Ewing's sarcoma and its clinical prognostic value.

Results: A total of 59 common differentially expressed FRGs were screened out. GO/KEGG enrichment and PPI network were executed. Based on 16 prognostic-related FRGs identified by univariate Cox regression in GSE17674, 2 molecular clusters were screened out via NMF consensus. Survival rate and immune infiltration were totally different in two clusters. Subsequently, multivariate/step Cox regression was conducted to identify 7 risk signatures (SLC2A1, PCK2, CHAC1, ATG13, PRKAA2, ARNT, and SIRT1). K-M survival (p = 1.785e-06) and ROC curves (with AUC value 0.816, 0877, 0.919 in 1, 3, 5 years) were plotted to assess the good predictive ability of risk model. ICGC dataset with K-M survival (p = 1.558e-02) and AUC value (0.886, 0.750, 0.709 in 1, 3, 5 years) was used to validate the risk model. Risk score and clinical features (gender, age stage status) were incorporated into a nomogram model. Immune microenvironment (IME) ingredients (ESTIMATE score, immune cells, immune-related pathways, and checkpoint genes) between two risk groups were also explored. High-risk group possessed an activated immune status compared to low-risk group. Finally,

Abbreviations: DEG, Differentially expressed genes; ES, Ewing's sarcoma; FRGs, ferroptosis-related genes; GO, Gene Ontology; ICGC, International Cancer Genome Consortium; KEGG, Kyoto Encyclopedia of Genes and Genomes; NMF, nonnegative matrix factorization; OS, Overall survival; ssGSEA, Single-sample gene set enrichment analysis.

Peer review under responsibility of Pontificia Universidad Católica de Valparaíso.

* Corresponding author.
E-mail address: 15153169737@163.com (Q. Li).

https://doi.org/10.1016/j.ejbt.2023.01.004

prognostic signatures exhibited perfect diagnostic ability in ES occurrence, and several drugs showed IC50 sensitivity to different risk groups.
Conclusions: Our study identified 7 prognostic signatures of FRGs and explored related immune infiltration which provided new aspects for future research in Ewing's sarcoma.
How to cite: Jiao X, Li Q, Xu X. Prognostic implication of a ferroptosis related gene signature associates with immunity in Ewing's sarcoma. Electron J Biotechnol 2023;64. https://doi.org/10.1016/j.ejbt.2023.01.004.

1. Introduction

Ewing's sarcoma (ES) is a primary bone sarcoma with an incidence of 3 per million in teenagers and adolescents [1]. Males tend to have a slightly higher incidence of ES compared to females, and common locations of ES include the metaphysis of limb bones. Spine and sacral lesions are often present in older patients. EWSR1 gene translocation progressing to EWS-FLI1 gene fusion in t(11; 22) is present in approximately 85-90% of ES cases [2]. Additionally, ES is highly susceptible to metastasis to the lungs in the early stages, with mortality rates within 5-year survival rates not exceeding 10% [3]. Therefore, there is an urgent need to identify biomarkers for early diagnosis and accurate prognostic prediction of ES patients.

Ferroptosis is a new mode of programmed cell death discovered in recent years. It is an oxidative cell death induced by small molecules in an iron-dependent manner [4]. Ferroptosis is mainly caused by the imbalance between the production and degradation of intracellular reactive oxygen species. Aberrant iron metabolism, reactive oxidative species generation, and abnormal lipid peroxidation are the hallmarks of ferroptosis [5,6]. Ferroptotic cells mainly exhibit severe damage in mitochondrial morphology: reduced volume, increased membrane density and decreased cristae [7]. Current research has demonstrated that ferroptosis is closely involved in tumor genesis, proliferation and metastasis. Eling et al. [8] found that artemisinin could activate ferroptosis in pancreatic cancer cells and inhibit the progression of pancreatic cancer. Louandre et al. [9] found sorafenib could promote the occurrence of ferroptosis in HCC cells with Rb-negative status. Also, erastin could induce gastric GC cell ferroptosis via cysteine dioxygenase type1 [10]. ROS accumulation caused by down-regulated SLC7A11 could induce ferroptosis in lung cancer cells [11]. Therefore, drugs based on ferroptosis will become a new target for tumor treatment in the future.

Recently, several studies have also investigated ferroptosis-related genes (FRGs) in tumors and developed potential prognostic models based on FRGs which effectively predicted the prognosis of tumors [12]. However, the role of FRGs in ES is limited. As such, we sought to identify prognostic FRGs signatures in this study to aid in the diagnosis and treatment of this disease.

2. Materials and methods

2.1. Data preparing

Two gene datasets, GSE17674 (GPL570) and GSE68776 (GPL5175) with corresponding clinical data, were obtained from the Gene Expression Omnibus database (https://www.ncbi.nlm.nih.gov/geo) via the "GEOquery" package. All gene probes were annotated with same criterion: probes matched several gene symbols were deleted and the maximum values were identified as gene expression when repetitive probes matched one gene symbol. GSE17674 [13] contains 44 ES samples with clinical information and 18 skeletal muscle set as training dataset. The GSE68776 [14] dataset contains 32 ES and 9 stem cells. We also downloaded mRNA expression profiles of 48 ES with clinical data from International Cancer Genome Consortium (ICGC) database (BOCA-FR) for test dataset. The expression profile of ICGC was transformed into log2+1 format for further study.

A total of 259 ferroptosis-related genes (FRGs, 108 driving genes/69 suppressor genes/ 111 markers) were collected from the ferroptosis database (http://www.zhounan.org/ferrdb).

The workflow chart is depicted in Fig. 1. Sample characteristics in two datasets are illustrated in Table 1.

2.2. Identification of differentially expressed FRGs, functional enrichment, PPI network

We used "limma" package to obtain the differentially expressed FRGs among different groups. We identified differentially expressed FRGs between 44 Ewing's sarcoma and 18 skeletal muscle samples in GSE17674 dataset, together with DE-FRGs between 32 Ewing's sarcoma and 9 stem cells in GSE68776 dataset. The criterion was set as an absolute value of |LogFC| >0.5 and adj.P.Val <0.05. Subsequently, we plotted Venn diagrams to visualize the common genes DE-RFGs by the intersection of differentially expressed FRGs in GSE68766 and GSE17674 for further survival study.

To further investigate the function of DE-FRGs, GO and KEGG enrichment were performed with "clusterProfiler" package [15]. We utilized the STRING (http://string-db.org/) to construct protein interaction networks based on DE-FRGs (minimum required interaction score >0.7).

2.3. Identification of prognostic-related FRGs and correlation

First, univariate Cox regression analysis was performed to determine prognostic-related FRGs (PR-FRGs) ($P < 0.05$) with "survival" package. In addition, correlation analysis with Pearson method was used to evaluate the relationships between PR-FRGs.

2.4. Consensus clustering analysis

Two molecular clusters with DE-CRG were identified according to nonnegative matrix factorization (NMF) clustering algorithm using "NMF" package [16]. Log-rank test was used to calculate the p-value and HR. Kaplan-Meier curves were plotted to compare the survival rate in different molecular clusters. The difference in infiltrating immune was evaluated between clusters.

2.5. Risk model construction and validation

Subsequently, multivariate Cox and step regression were performed to screen out the risk signature with the lowest Akaike's information criterion utilizing "survminer" package [17]. Eventually, the risk score of each sample was calculated: risk score = Ei

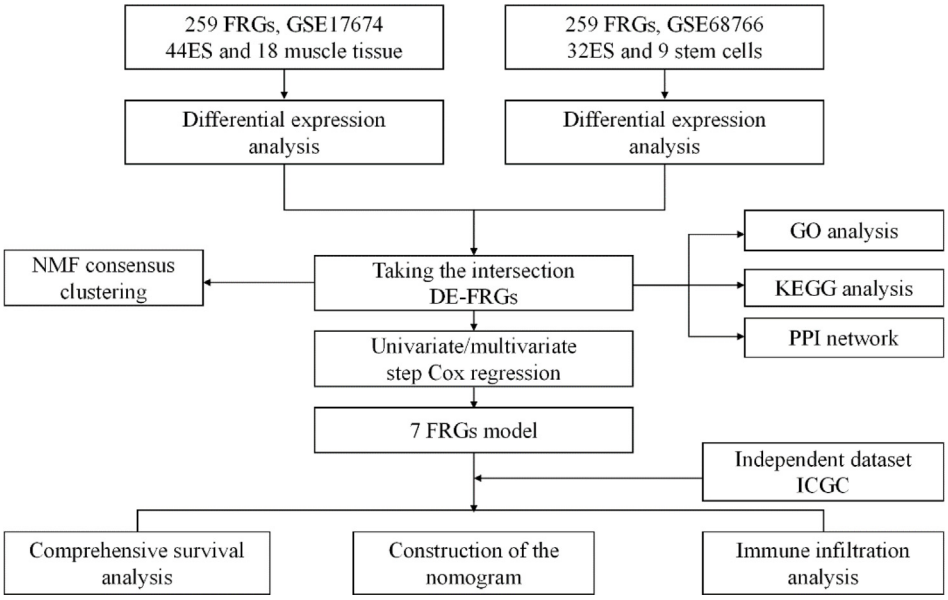

Fig. 1. Workflow chart of data analysis.

Table 1
The ES samples in training and test datasets

Variables	GSE17674 dataset	ICGC dataset
Numbers	44	48
Age, years (%)		
≥14	33 (82.81%)	32 (66.67%)
<14	11 (17.19%)	16 (33.33%)
Gender (%)		
Female	20 (31.25%)	21 (43.75%)
Male	44 (68.75%)	27 (56.25%)
Survival status (%)		
Alive	24 (37.5%)	26 (54.17%)
Dead	40 (62.5%)	22 (45.83%)
Stage (%)	32 (72.7%)	34 (70.83%)
Primary	12 (27.3%)	13 (27.08%)
Metastasis/Recurrence		1 without Stage

coefficient (gene)×expression (gene). We set the median value of risk score as the cut point; all samples were divided into two groups: high risk and low risk. The distribution of risk score and survival state was determined. The PCA analysis was conducted with "scatterplot3d" package. Kaplan-Meier survival method, time-dependent receiver operating characteristic (ROC) and C-index were plotted to evaluate the efficiency of prognostic risk model.

Additionally, the ICGC dataset was set as external test dataset for further validation of the performance of risk signatures.

2.6. Nomogram construction and validation

To assess the independence of risk model for samples, clinical data (including gender, age, stage status) and risk score were evaluated by univariate and multivariate Cox regression. Utilizing "rsm" package, nomogram was established, which was employed for predicting the survival of ES. Finally, calibration curves were used to assess the accurateness of the 1, 3, 5 years of prediction.

2.7. Immune infiltration analysis

We evaluated the overall level of immune infiltration by ESTIMATE algorithm [18]. ssGSEA algorithm was used to evaluate the difference between high- and low-risk groups in the infiltration of 28 immune cells. $P < 0.05$ suggested an accurate estimation. We also accessed the 13 immune functions and the expression level of 10 checkpoints (CD40, LGALS9, TMIGD2, ICOSLG, TNFRSF4, LAIR1, CD48, TNFSF15, KIR3DL1, and BTNL2) in different risk groups.

2.8. Diagnostic ability of risk signatures and drug sensitivity

For further understanding the predictability of risk signatures in the occurrence of ES, ROC curves with AUC value were drawn, and we validated them in GSE68776 dataset.

The "pRRophetic" package [19] was used to explore the half-maximal inhibitory concentration (IC50) of chemotherapy drugs between different risk groups. We downloaded all cell line expression data from Genomics of Drug Sensitivity in Cancer (GDSC) (www.cancerrxgene.org) and compared with expression profile of training dataset. Finally, based on IC50 of chemotherapy drugs predicted, we demonstrated the drugs were potentially benefited to samples in different risk groups.

3. Results

3.1. Differentially expressed FRGs (DE-FRGs) identification, functional enrichment, and PPI Network

A total of 140 differentially expressed FRGs were identified in GSE17674, together with 95 differentially expressed FRGs in GSE68766. The volcano and heatmap were displayed in Fig. 2a,b,c,d. Subsequently, we got 59 common DE-FRGs by the intersection of two differentially expressed FRGs for further study. The common DE-FRGs were displayed by Venn plot in Fig. 2f.

The functional enrichment of 59 DE-FRGs provided a biological understanding of these genes and were displayed in Fig. 2e. The biological process was remarkably involved in response to nutrient levels, response to oxidative stress, and cellular response to chemical stress. Cellular component analysis suggested that the apical part of cell, membrane raft, and membrane microdomain were mainly enriched. The results of molecular function were majorly located in antioxidant activity, long-chain fatty acid-CoA, and ligase activity. KEGG showed that these genes were mainly associated with autophagy-animal, FoxO signaling pathway, chemical carcinogenesis-reactive oxygen species and ferroptosis. The PPI

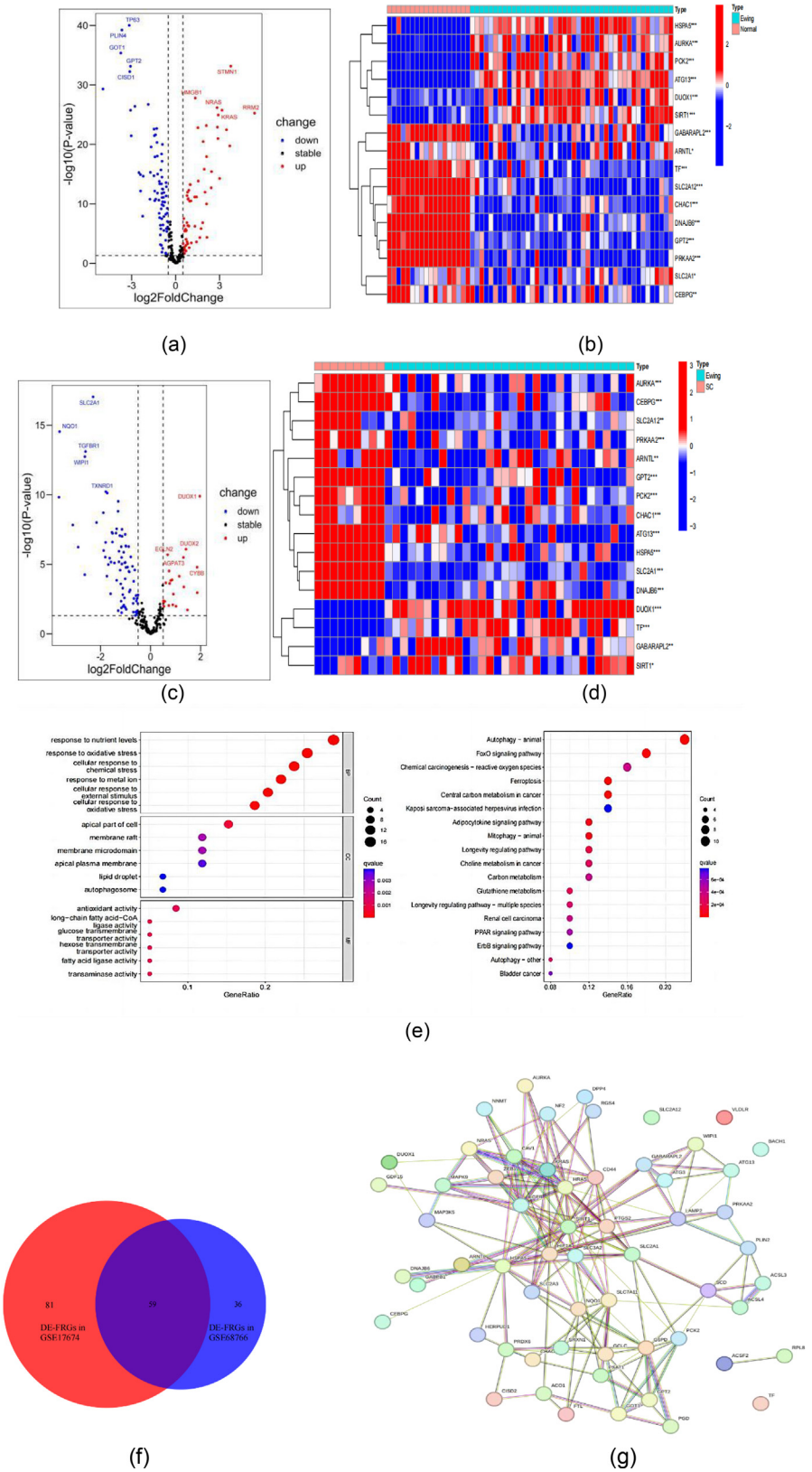

Fig. 2. DE-FRGs identification, functional enrichment, and PPI network: (a,b) Volcano plot of DE-FRGs and heatmap of PR-FRGs in GSE17674; (c,d) Volcano plot of DE-FRGs and heatmap of PR-FRGs in GSE68766; (e) The results of GO and KEGG analysis; (f) Venn diagram showing the 59 intersectional genes between two DE-FRGs; (g) PPI network of 59 DE-FRGs.

network of 59 DE-FRGs created with the minimum required interaction score >0.4 is present in Fig. 2g.

3.2. Identification of prognostic-related FRGs and correlation

We evaluated 59 DE-FRGs by univariate Cox regression analysis and identified 16 genes as prognostic-related FRGs (PR-FRGs). The forest map showed the hazard ratio of 16 PR-FRGs in Fig. 3a, green indicated protect factor, while red indicated risk factor. The correlations of 16 PR-FRGs were explored to further understand their interactions. Fig. 3c revealed that there was a close correlation between the expressions of the 16 PR-FRGs. For instance, SIRT1 was negatively correlated with DUOX1 (r = 0.56), while TF1 was positively correlated with PCK2 (r = −0.55).

3.3. Classification of molecular clusters

On the basis of the 16 PR-FRGs, two molecular clusters (C1 = 23, C2 = 21) were identified by NMF consensus. PCA was used to validate the two molecular clusters. We found that C2 had a better overall survival than C1 (p = 9.055e-03). The heatmap and boxplot showed that the C1 samples and C2 samples had different expression levels of FRGs.

We found that immune cells, such as activated CD4 T cell, activated CD8 T cell, natural killer T cell, and type 2 T helper cell, were all significantly up-regulated in C1, and C1 was also abundant in APC-co-stimulation, T-cell-co-inhibition, and checkpoint genes LAIR1, and BTNL2 (Fig. 4).

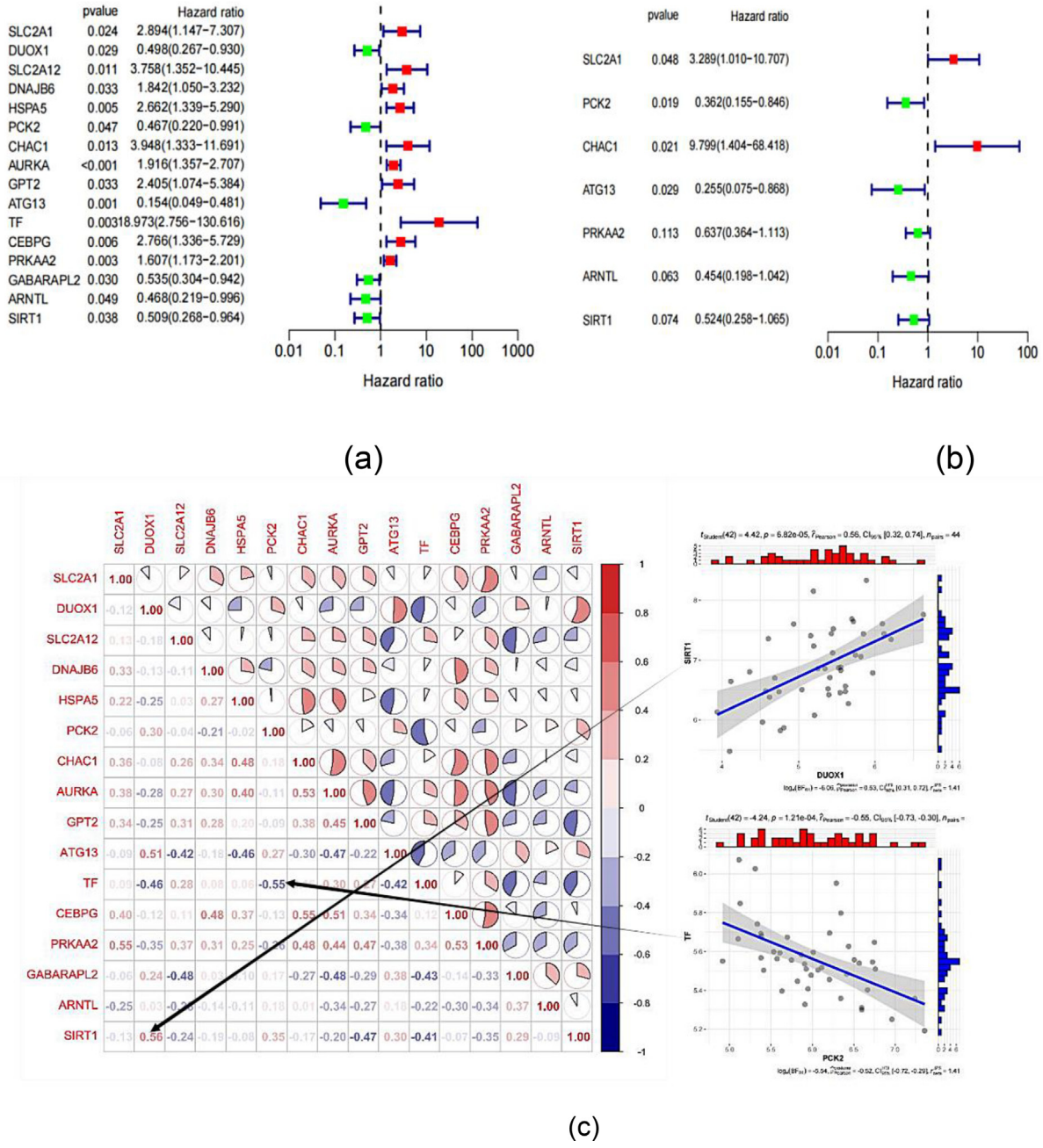

Fig. 3. Identification of prognostic-related FRGs and correlation: (a,b) The hazard ratio forest map of univariate and step regression; (c) Correlation of PR-FRGs.

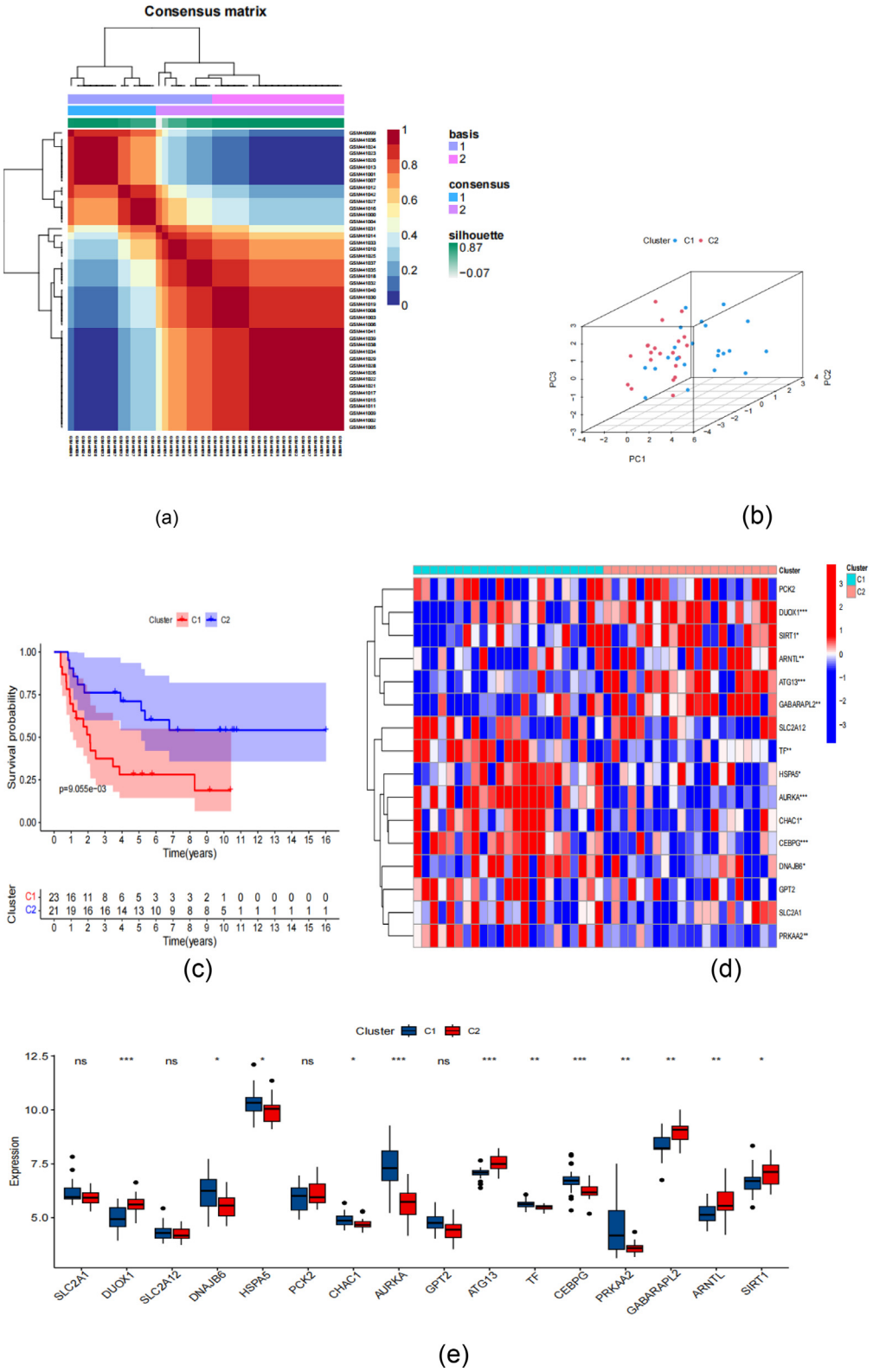

Fig. 4. Two molecular clusters identified by NMF consensus: (a) Two molecular clusters based on 16 PR-FRGs; (b) PCA result of two clusters; (c) Kaplan-Meier survival curves between molecular clusters; (d,e) Heatmap and boxplot of DE-FRGs between molecular clusters; (f,g) Heatmap and boxplot of immune cells between molecular clusters; (h,i) Boxplot of immune pathways and checkpoints between molecular clusters. (“****”, “***”, “*”, “ ”, P = 0, 0.001, 0.01, 0.05, 1).

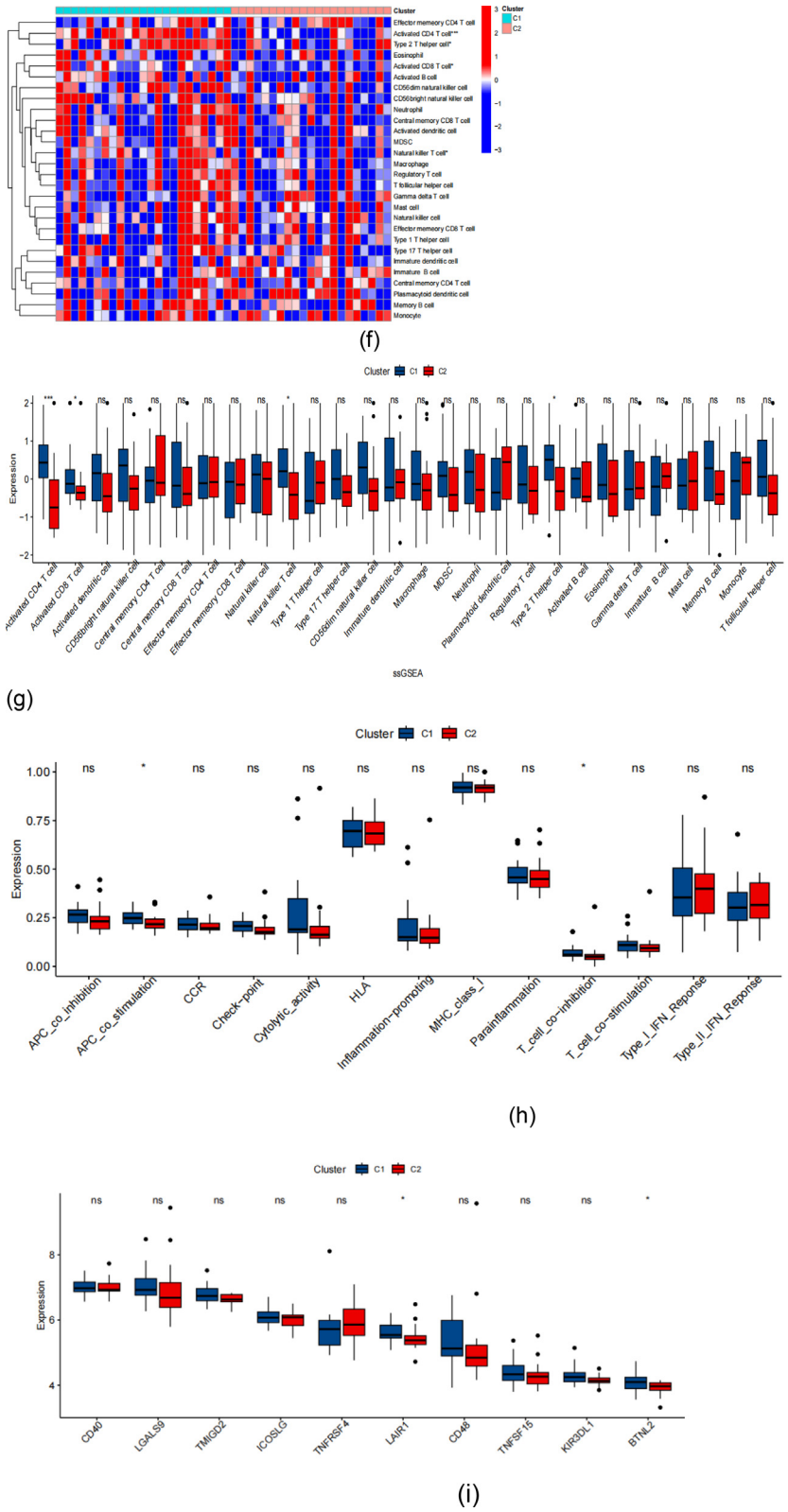

Fig. 4 (*continued*)

3.4. Construction of risk model based on FRGs

Subsequently, multivariate Cox and step regression were conducted, 7 FRGs (SLC2A1, PCK2, CHAC1, ATG13, PRKAA2, ARNT, SIRT1) with the lowest AIC were generated as the prognostic signature. Forest map was used to visualize the risk model in Fig. 3b. According to the hazard ratio of 7 signatures, SLC2A1 and CHAC1 were regarded as risk factors while PCK2, ATG13, PRKAA2, ARNT, and SIRT1 were protect variables. Additionally, SLC2A1, PCK2, CHAC1, ATG13 in 7 signatures were statistically significant with

$p < 0.05$, indicating them were independent prognostic indicators. Risk score formula was determined: risk score = SLC2A1*1.91 + PCK2*-1.017 + CHAC1*2.282 + ATG13*-1.368 + PRKAA2*-0.451 + ARNTL*-0.789 + SIRT1*-0.646. According to the median risk scores, we stratified 44 ES samples into high- and low-risk groups. The distribution of risk score, survival status was shown in Fig. 5a,b. It reflected samples in different groups with different prognoses. The PCA showed a clear separation in two risk groups. Kaplan-Meier method indicated the survival rate of high-risk group was significantly lower than low-risk groups ($p < 0.001$). The AUC value of ROC curves was 0.816, 0.879, 0.921 in 1, 3, 5 years, respectively. Heatmap displayed the relationship between clinical features of ES and the expression of risk signature in Fig. 5f. Except for PCK2, the expression levels of 6 signatures, SLC2A1, CHAC1, ATG13, PRKAA2, ARNTL and SIRT1 in different risk groups, are significant differences ($p < 0.05$) in Fig. 5g. We found that there was a close positive correlation among SLC2A1, CHAC1, and PRKAA2 in Fig. 5h.

3.5. Validation of the prognostic signature

Moreover, the prognostic model was verified by ICGC dataset. The samples in ICGC were also divided into high- and low-risk groups according to median risk scores. Kaplan-Meier method revealed that high-risk group had a worse survival rate ($p = 1.588e-02$) in Fig. 6c. The AUC values under ROC curves were 0.886, 0.750, 0.709 in 1, 3, 5 years respectively in Fig. 6d. The expression levels of SLC2A1 CHAC1 and ATG13 in groups were significant difference. As in GSE17674 dataset, SLC2A1, CHAC1, and PRKAA2 also showed a close positive correlation between each other in Fig. 6h. These indicated that the prognostic model exhibited excellent performance in prognostic prediction.

3.6. Clinical features associated with risk model

Survival analysis was further applied to clinical subgroups in GSE17674 dataset. Our data indicated that the risk model showed excellent performance in predicting outcome in age $\geq$ 14 years ($p < 0.001$), age <14 years ($p = 0.056$), female ($p < 0.001$), male ($p = 0.001$), stage-primary ($p = 0.001$), stage metastasis ($p < 0.001$) in Fig. 7a.

Compared with clinical features (sex, age, stage), risk score had the highest AUC values in 1, 3, 5 years in Fig. 7b. The C-index of risk score also was higher than all clinical features (sex, age, stage) in Fig. 7c. Fig. 7d displayed the relationship of molecular clusters, risk groups and clinical features. These above results illustrated the excellent predictive ability of risk score.

3.7. Establishment and validation of nomogram

As shown in Fig. 8a, the risk score was an independent prognostic factor demonstrated by univariate and multivariate Cox regression with $P < 0.05$, no prognosis association with clinical features: gender, age, and stage. Subsequently, we incorporated risk level and clinical features (sex, age, stage) to construct a nomogram model to predict the rates of overall survival in 1, 3, 5 years in Fig. 8b. The result of calibration curves indicated high efficiency of nomogram Fig. 9d.

Meanwhile, nomogram in ICGC dataset was also constructed. Calibration curves showed its good predictive accuracy for the survival prognosis of ES in Fig. 9c,e.

3.8. Immune infiltration analysis

The ESTIMATE algorithm illustrated higher stromal score in low-risk group (Fig. 10a). Subsequently, ssGSEA analysis was used to evaluate the abundance of diverse immune cells. The result revealed that central memory CD4 T cell, immature B cell were significantly enriched in the low-risk group, but the high-risk group had a significant abundance of activated CD4 T cell, activated CD8 T cell, CD56dim natural killer cell in Fig. 10b,c,d,e,f,g,h. Fig. 10i revealed that risk score was negatively correlated with the abundance of most immune cells. High-risk group exhibited a higher level of T cell co-inhibition Fig. 10j. The immune checkpoint genes, CD40 and TMIGD2, were highly expressed in high-risk group ($p < 0.05$) in Fig. 10i. Risk signatures were correlated with immune cells, such as CHAC1 was positively related to activated CD4 T cell ($r = 0.63$), while SIRT1 was negatively correlated with CD56dim natural killer cell ($r = -0.54$).

3.9. Diagnostic ability of risk signatures and drug sensitivity

We studied the predictability of risk signatures in occurrence of ES. The AUC values of SLC2A1, PCK2, CHAC1, ATG13, PRKAA2, ARNTL, and SIRT1 were 0.664, 0.979, 0.984, 1, 1, 1, and 0.915, respectively. We validated them in GSE68776, and the AUC values of SLC2A1, PCK2, CHAC1, ATG13, PRKAA2, ARNTL, and SIRT1 were 1, 1, 0.861, 0.969, 0.854, 0.799, and 0.711, respectively.

We explored drug sensitivity between different risk groups via "pRRophetic" package. The result demonstrated that low-risk group was predicted to benefit from ABT.263, AICAR, KU.55933, RO.3306, and SL.0101.1, while high-risk group benefited more from AKT-inhibitor-VIII, AP.24534, AS601245, AZD6482, Bexarotene, Bleomycin, CCT007093, CHIR.99021, FTI.277, Imatinib, JNK.9L, MG.132, Midostaurin, and PF.562271.

4. Discussion

Ewing's sarcoma is one of the most aggressive bone sarcomas. Studies report that the 5-year survival rate of ES is from 65% to 80%. It decreased to 30% after recurrence and metastases [20]. Early diagnosis and appropriate treatment could significantly improve the 5-year survival rate [21]. Ferroptosis as a new form of cell death plays an important anti-cancer role in colorectal cancer [22], gastric cancer [10] and hepatocellular carcinoma [9]. Potential prognostic biomarkers based on FRGs are identified in various types of human cancer. However, there has little study reported to comprehensive analysis of the relationship between ferroptosis and clinical features in ES.

In the current work, we first screened out 59 FRGs that were differentially expressed between ES and normal tissues. Functional enrichment uncovered that these genes were remarkably involved in response to nutrient levels/ oxidative stress, apical part of cell, membrane raft, membrane microdomain antioxidant activity, long-chain fatty acid-CoA. KEGG showed that these genes were mainly associated with autophagy-animal, FoxO signaling pathway, chemical carcinogenesis-reactive oxygen species and ferroptosis. These pathways were closely related to the biological behaviors of various tumors, which suggested that dysfunction of ferroptosis was crucial in the development of ES. Based on 16 PR-FRGs identified by univariate Cox regression, two molecular clusters were identified via NMF consensus. Kaplan-Meier survival curves display the overall survival time was worse in C1 than in C2. Analysis of immune infiltration indicated that C1 was charactered by activated immunity status, such as immune cells: activated CD4 T cell, activated CD8 T cell, natural killer T cell, and type 2 T helper cell, immune pathways and checkpoints: APC-co-stimulation, T-cell-co-inhibition, LAIR1, and BTNL2. We conclude activated immunity status but worse survival rates in C1.

Finally, 7 genes were screened out by step regression with the lowest AIC to construct the risk model. The outcomes of Kaplan-Meier and ROC curves exhibited the good predictive ability of risk

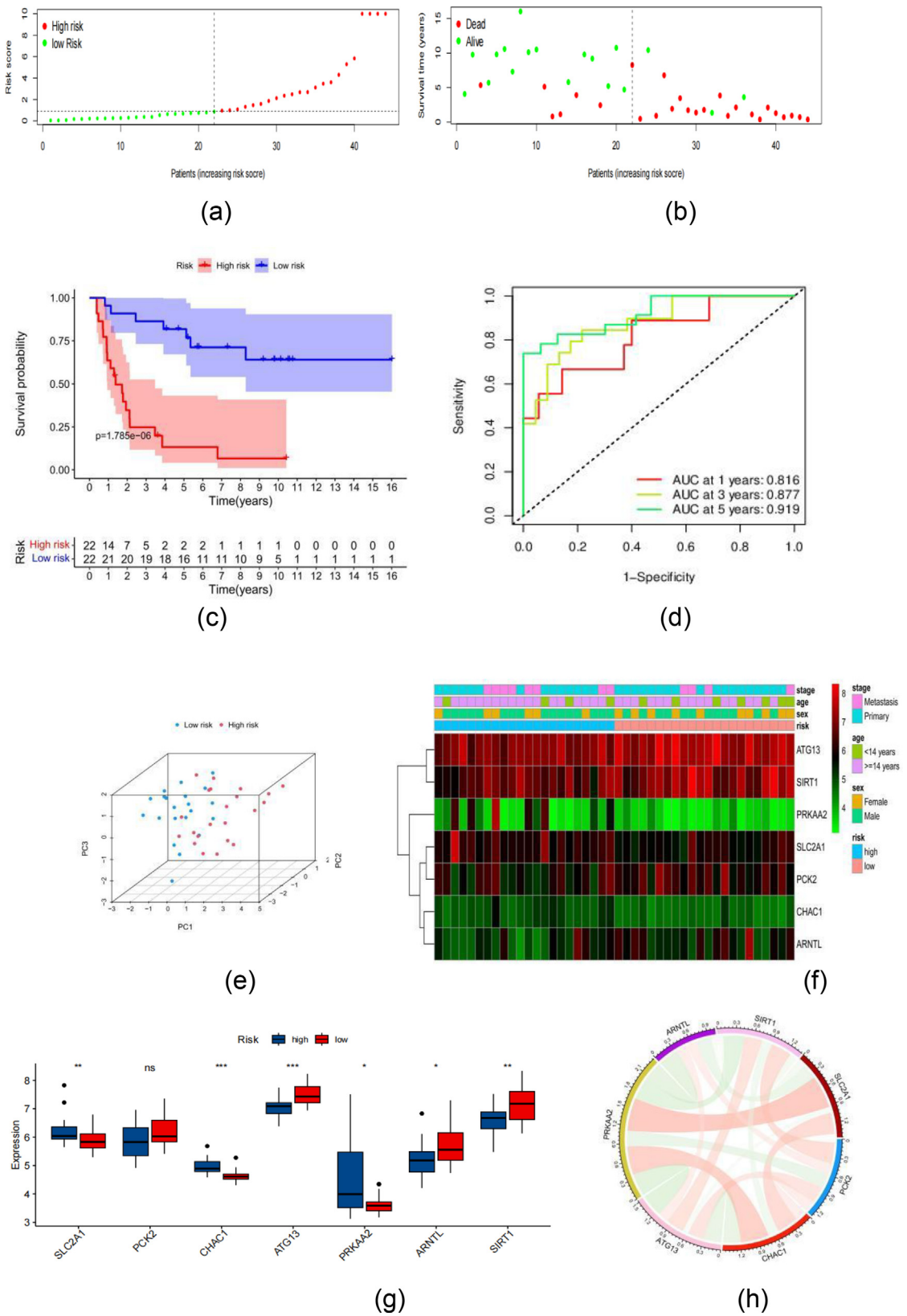

Fig. 5. Prognostic value of 7 FRG signatures in training dataset: (a, b, c, d, e, f, g, h) Distribution of the risk score, survival status, K-M survival analysis, time-ROC analysis, PCA analysis, heatmap of the FRGs signature, boxplot of the FRGs signature (“****”, “**”, “*”, “ ”, P = 0, 0.001, 0.01, 0.05, 1) and correlation of FRGs signatures (red: positive correlation, green: negative correlation).

model in training and validation datasets. Zhao et al. [23] reported a risk model based on three FRGs (AURKA, RGS4, and RIPK1) which was different from ours. The AUC values in 1, 3, 5 years were 0.81, 0.79, and 0.74 in training dataset, and 0.70, 0.67, 0.61 in GSE63157, and 0.770, 0.770, 0.663 in SRAC dataset. Our proposed signatures had higher AUC: 0.816, 0.877, and 0.919 in GSE17674, and 0.886,

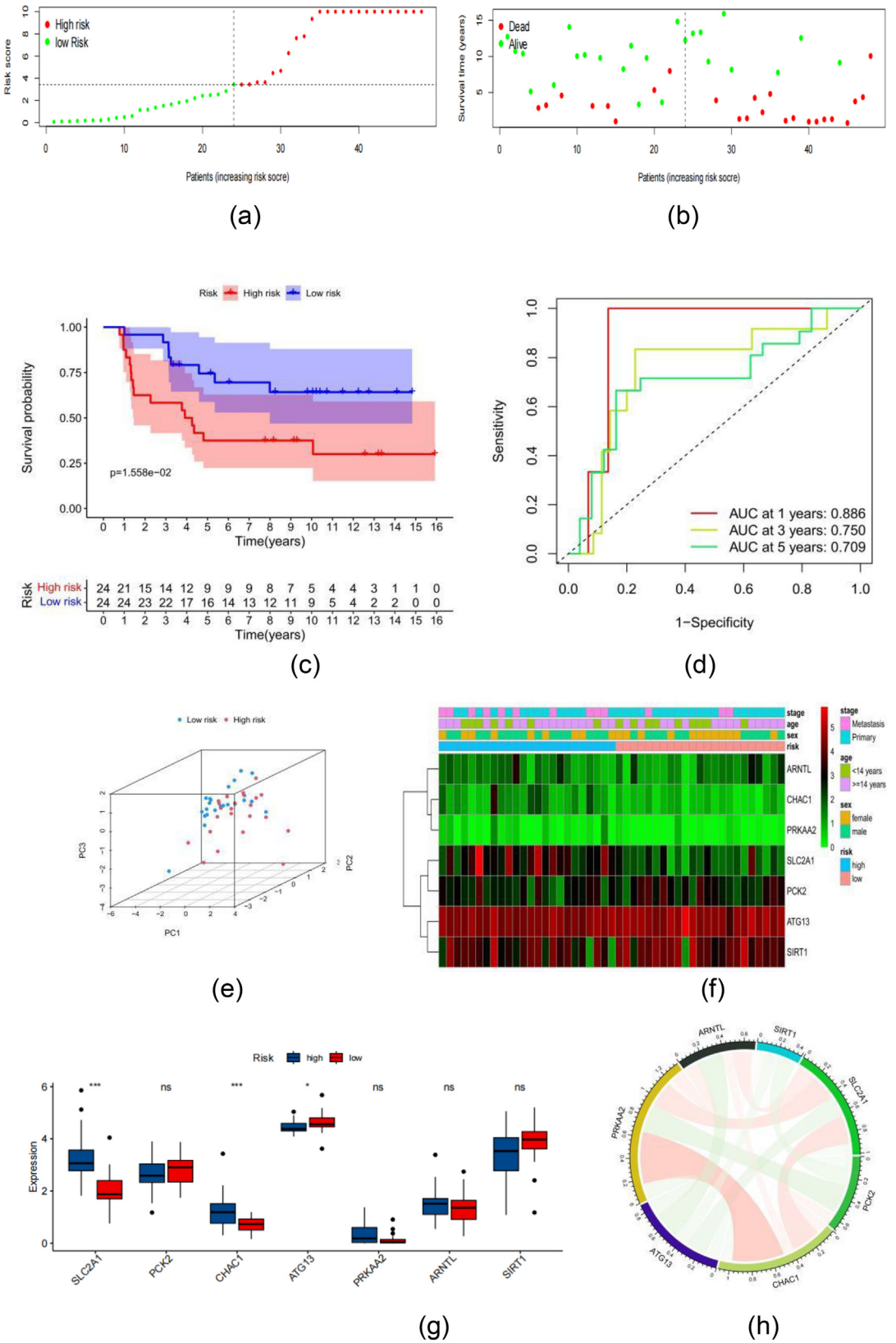

Fig. 6. Prognostic value of 7 FRG signatures in ICGC. (a, b, c, d, e, f, g, h) Distribution of the risk score, survival status, K-M survival analysis, time-ROC analysis, PCA analysis, heatmap of the FRGs signature, boxplot of the FRGs signature (“****”, “***”, “**”, “*”, “ ”, P = 0, 0.001, 0.01, 0.05, 1) and correlation of FRGs signatures (red: positive correlation, green: negative correlation).

0.750, 0.709 in ICGC, which indicates high diagnostic value. Clinical subgroup analysis demonstrated that the risk model also exhibited great efficiency in different clinical subgroups. Then, we demonstrated risk score was an independent prognostic factors, not affected by clinic features (sex, age, stage) by univariate and multivariate regression. Nomograms were constructed based on risk

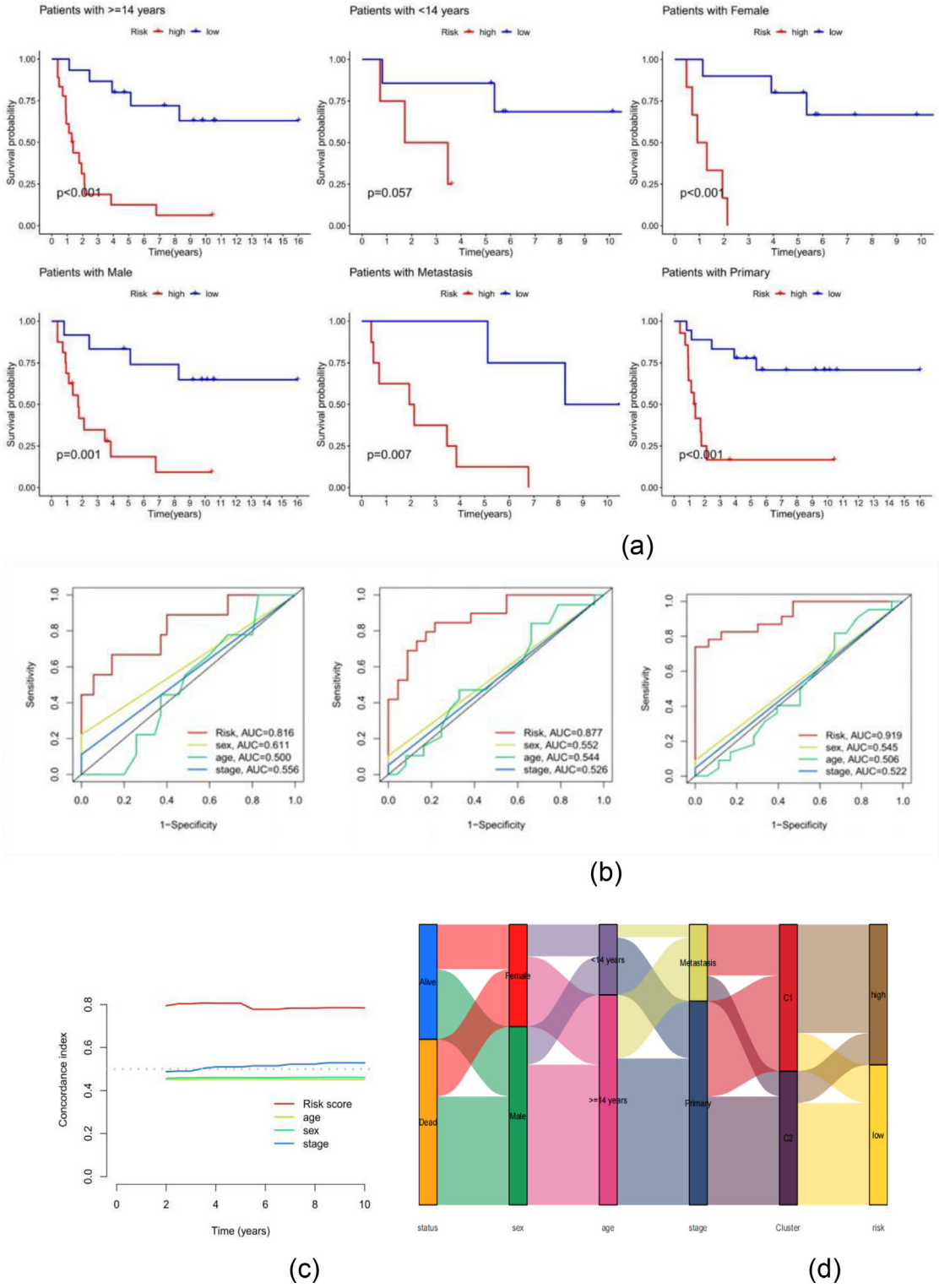

Fig. 7. Subgroup survival analysis in GSE17674: (a)K-M survival analysis of clinical subgroups: age, sex, stage; (b) ROC of risk score and clinical features (sex, age, stage) in 1, 3, 5 years; (c) C-index of risk score and clinical features (gender, age, stage). (k) Alluvial diagram of molecular cluster, risk group and clinical features.

level and clinical features in GEO and ICGC datasets. Calibration curves in 1, 3, and 5 years demonstrated that the nomograms had a high prognostic predictive value. Interestingly, we found that risk signatures exhibited well in the diagnostic occurrence of ES. Drug sensitivity was also done to explore the IC50 of chemical drugs between risk groups.

This ferroptosis-based risk model was composed of 7 FRGs: SLC2A1, PCK2, CHAC1, ATG13, PRKAA2, ARNTL, and SIRT1. These 7 signatures were related to the oncogenesis and progression of different types of cancer, and their biological behavior in tumor had been widely reported. SLC2A1 encodes the glucose transporter GLUT1, which promotes glycolysis and proliferation and migration

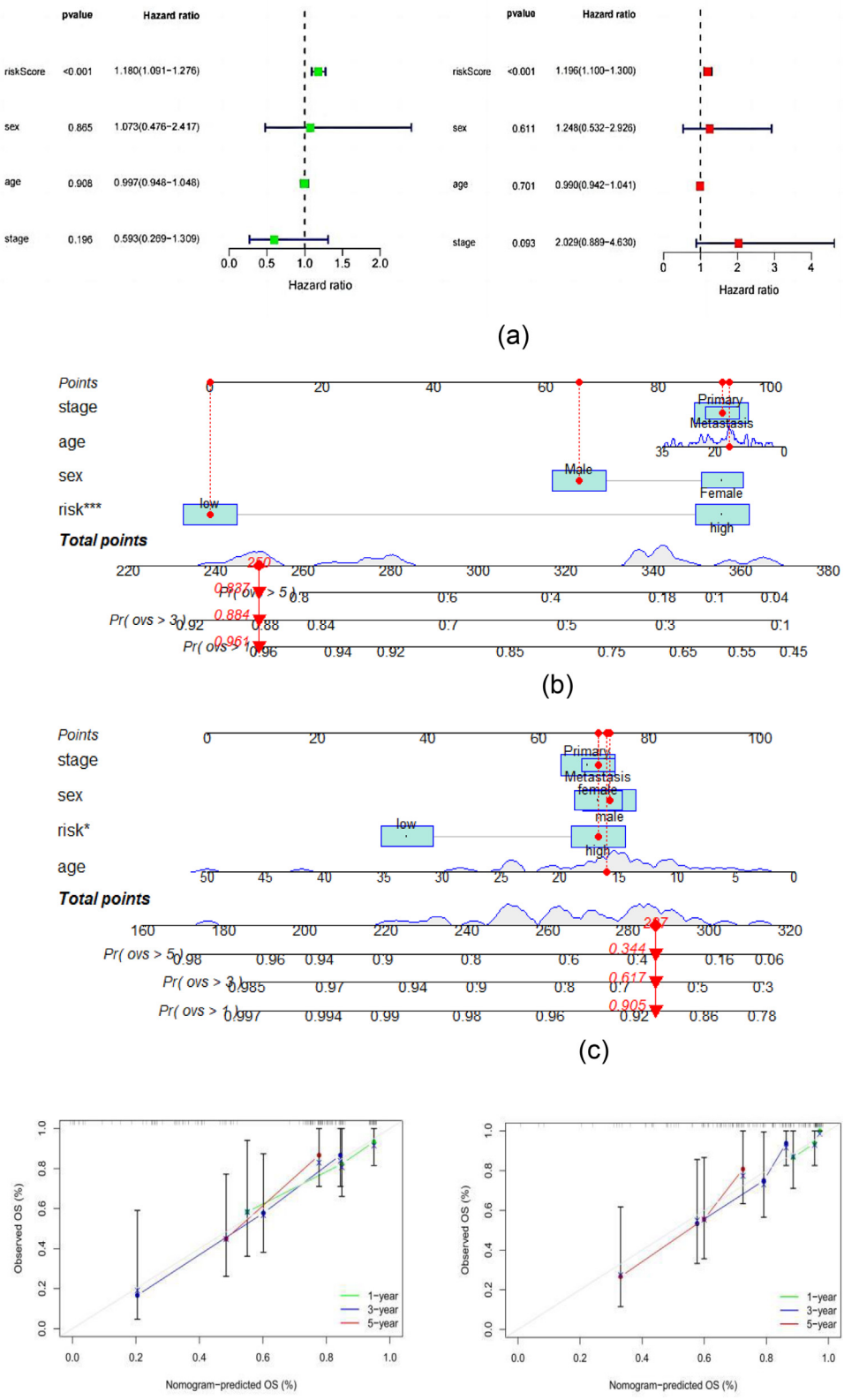

Fig. 8. Establishment and validation of nomogram: (a) Independence results of univariate and multivariate regression; (b,c) Nomogram in GSE17674 and ICGC; (d,e) the calibration plots for predicting 1, 3, 5 years OS in GSE17674 and ICGC.

of various tumors [24]. Min et al. [25] revealed that up-regulated SLC2A1 could lead to cancer cell proliferation, decreased immune cell infiltration and a low prognostic nutrition index in gastric cancer. Guo W et al. also demonstrated that up-regulated SLC2A1 was significantly related to poor prognosis, low immune infiltration in LUAD and CRC [26]. We found that SLC2A1 was downregulated in ES samples and acted as a risk factor in oversurvival. PCK2 inhibits the proliferation of lung cancer cells by acting as a regulator of

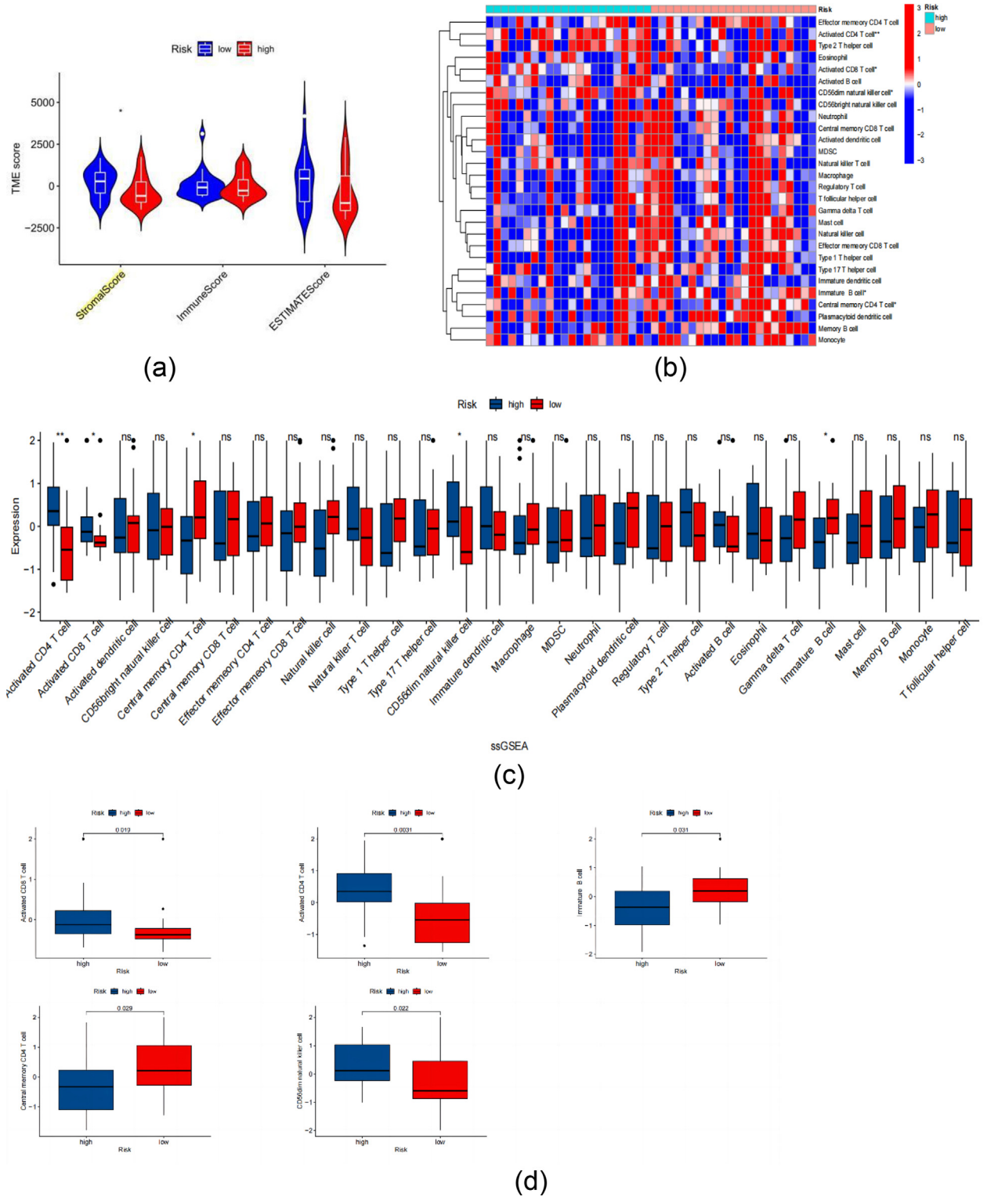

Fig. 9. The results of immune infiltration analysis: (a) Violin plot of ESTIMATE Score between different risk groups; (b,c,d) Heatmap, and boxplot of immune cells between different risk groups; (e, f) Boxplot of immune-related pathways and checkpoints between different risk groups; (i) Correlation of risk signatures and immune cells (“****”, “***”, “**”, “ ”, P = 0, 0.001, 0.01, 0.05, 1).

mitochondrial respiration to reduce glutathione production [27]. Meanwhile, PCK2 was also reported as a protective factor in breast cancer [28]. Chao C et al. showed that PCK2 was able to reduce cancer stemness, thereby inhibiting the progression of BLBCs [29]. Our present study reinforced that PCK2 acted as a suppressor in the progression of various tumors, including ES. Goebel et al. [30] reported found that CHAC1 was up-regulated in patients with poor prognosis in breast and ovarian cancers. CHAC1 promoted ferroptosis via the GCN2-eIF2α-ATF4 pathway in TNBC [31]. Our risk model indicated that CHAC1 was a risk prognostic biomarker for ES. As the most crucial substrates of TORC1, ATG13 plays an important role of autophagy regulators. Research shows that targeting

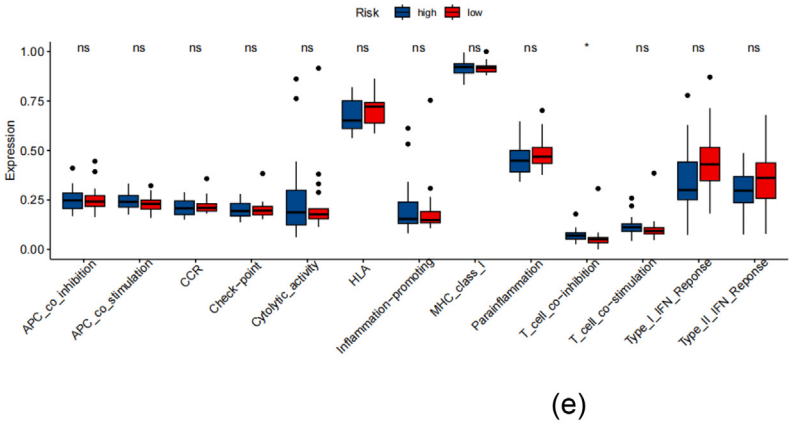

(e)

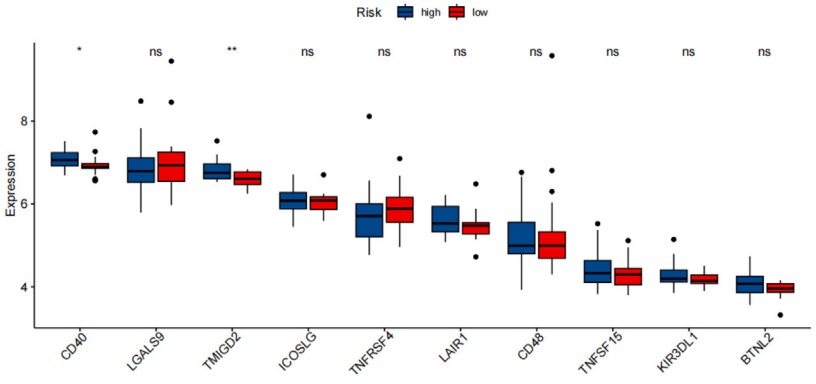

(f)

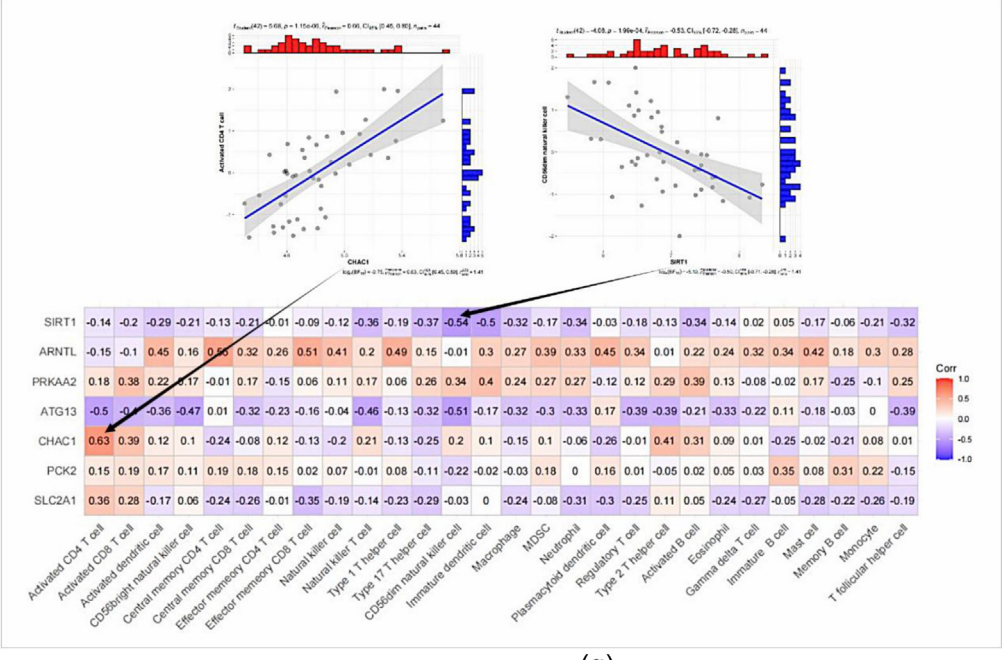

(g)

Fig. 9 (*continued*)

ATG13 inhibits the autophagy-mediated proliferation of colorectal cancer [32]. Niu et al. [33] reported that ATG13 could induce autophagy-mediated apoptosis of hepatocellular carcinoma. Our results suggested that ATG13 may act as a risk factor in ES prognosis. PRKAA2 induced sustained phosphorylation of p53, and accelerated cellular senescence to inhibit cell proliferation [34]. PRKAA2 was also proved as a tumor repressor in CRC [35]. Down-regulated PRKAA2 leads tumor cell proliferation and larger xenografts in bladder cancer [36]. Liu et al. [37] reported that ARNTL acted as a regulator of circadian clock to promote lipid peroxidation and

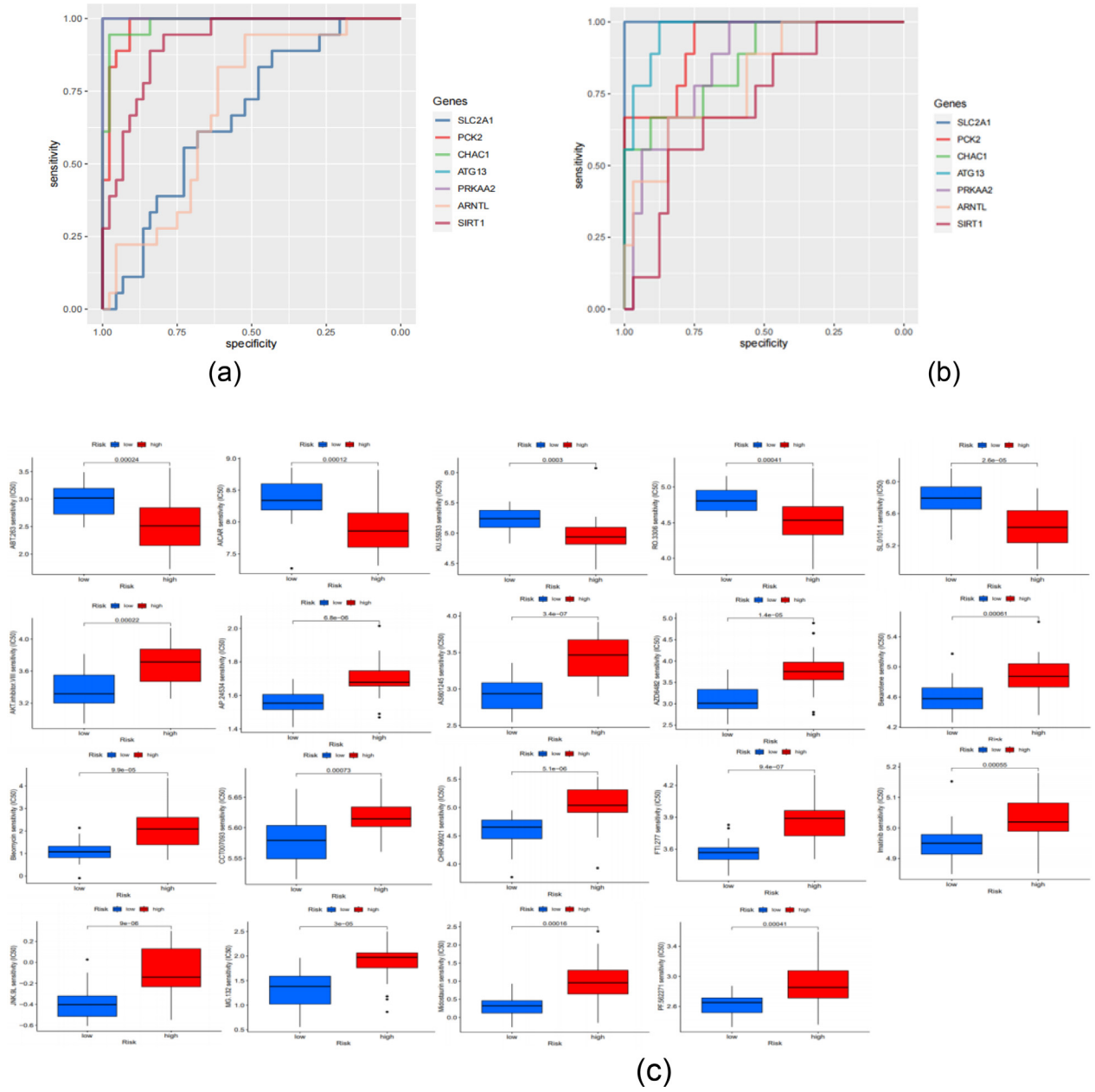

Fig. 10. Diagnostic ability of risk Signatures and drug sensitivity: (a, b) ROC curves of risk signature in training and GSE68776 datasets; (c) Result of drug sensitivity between different risk groups.

induce cell ferroptosis. Yeh et al. [38] demonstrated that the high level of ARNTL restored c-MYC rhythm and service as a tumor suppressor in ovarian cancer. In our risk model, PRKAA2 and ARNTL acted as tumor suppressors and could be prognostic biomarkers for ES. SIRT1 is a member of the sirtuin family and services as a tumor suppressor in gastric cancer through STAT3-MMP-13 axis [39]. But Chen et al. [40] reported that SIRT1 up-regulates the expression of GLUT1, and promotes the proliferation of bladder cancer cells. In our risk model, SIRT1 was a risk prognostic factor. SIRT1 may play different roles in different cancers. The mechanism of SIRT1 in various types of cancers needs further study.

Previous studies addressed a close connection between prognosis and immunity in various tumors [41], so we explored immune infiltration in risk model. Our study revealed that the low-risk group had a higher stromal score. In ssGSEA, the high-risk group had a significant abundance of activated CD4 T cell, activated CD8 T cell, CD56dim natural killer cell. Immune-related pathways and checkpoint genes, such as T cell co-inhibition, CD40 and TMIGD2, were also highly expressed in high-risk group. The significant difference in immune infiltration in risk groups suggested ferroptosis might affect ES by influencing immune infiltration. Similar to infiltration immunity in molecular clusters, we conclude activated immunity status but worse survival rates in high-risk group and molecular C1. The problem faced by researchers was how to activate these immune cells to eliminate malignant cells in ES. The result paved the ways for immunotherapy in ES and remained to be validated by future study.

We admitted certain limitations in the above work. First, due to the rarity of ES, the number of samples in 2 datasets (GSE17674 and ICGC) in this study is still small. Second, only public datasets have been used in our study, additional external data and experiments are needed to further verify our results. The potential mech-

anism of FRGs in the prognosis of ES needs further study to be demonstrated.

5. Conclusions

Our study identified 7 prognostic signatures of ferroptosis-related genes in ES, and developed a successful predict risk model based on RFGs. Our study provides new aspects for future research on ES.

Author contributions

- Study conception and design: Q Li; X Jiao
- Data collection: X Xu
- Analysis and interpretation of results: X Jiao; X Xu; Q Li
- Draft manuscript preparation: X Jiao; Q Li
- Revision of the results and approval of the final version of the manuscript: X Jiao; X Xu; Q Li

Financial support

The study received no external funding.

Conflicts of interest

The authors declare no conflicts of interest.

Data availability

The data used in this study are available publicly in GEO (https://www.ncbi.nlm.nih.gov/geo) and ICGC (https://dcc.icgc.org).

References

[1] Grünewald TGP, Cidre-Aranaz F, Surdez D, et al. Ewing sarcoma. Nat Rev Dis Primers 2018;4(1):5. https://doi.org/10.1038/s41572-018-0003-x. PMid: 29977059.
[2] Delattre O, Zucman J, Plougastel B, et al. Gene fusion with an *ETS* DNA-binding domain caused by chromosome translocation in human tumours. Nature 1992;359(6391):162–5. https://doi.org/10.1038/359162a0. PMid: 1522903.
[3] Iwamoto Y. Diagnosis and treatment of Ewing's sarcoma. Jpn J Clin Oncol 2007;37(2):79–89. https://doi.org/10.1093/jjco/hyl142. PMid: 17272319.
[4] Dixon SJ, Lemberg KM, Lamprecht MR, et al. Ferroptosis: an iron-dependent form of nonapoptotic cell death. Cell 2012;149(5):1060–72. https://doi.org/10.1016/j.cell.2012.03.042. PMid: 22632970.
[5] Zuo S, Yu J, Pan H, et al. Novel insights on targeting ferroptosis in cancer therapy. Biomarker Res 2020;8:50. https://doi.org/10.1186/s40364-020-00229-w. PMid: 33024562.
[6] Mou Y, Wang J, Wu J, et al. Ferroptosis, a new form of cell death: opportunities and challenges in cancer. J Hematol Oncol 2019;12(1):34. https://doi.org/10.1186/s13045-019-0720-y. PMid: 30925886.
[7] DeHart DN, Fang D, Heslop K, et al. Opening of voltage dependent anion channels promotes reactive oxygen species generation, mitochondrial dysfunction and cell death in cancer cells. Biochem Pharmacol 2018;148:155–62. https://doi.org/10.1016/j.bcp.2017.12.022. PMid: 29289511.
[8] Eling N, Reuter L, Hazin J, et al. Identification of artesunate as a specific activator of ferroptosis in pancreatic cancer cells. Oncoscience 2015;2(5):517–32. https://doi.org/10.18632/oncoscience.160. PMid: 26097885.
[9] Louandre C, Marcq I, Bouhlal H, et al. The retinoblastoma (Rb) protein regulates ferroptosis induced by sorafenib in human hepatocellular carcinoma cells. Cancer Lett 2015;356(2 Pt B):971–7. https://doi.org/10.1016/j.canlet.2014.11.014. PMid: 25444922.
[10] Hao S, Yu J, He W, et al. Cysteine dioxygenase 1 mediates erastin-induced ferroptosis in human gastric cancer cells. Neoplasia 2017;19(12):1022–32. https://doi.org/10.1016/j.neo.2017.10.005. PMid: 29144989.
[11] Wang LL, Luo J, He ZH, et al. STEAP3 promotes cancer cell proliferation by facilitating nuclear trafficking of EGFR to enhance RAC1-ERK-STAT3 signaling in hepatocellular carcinoma. Cell Death Dis 2021;12(11):1052. https://doi.org/10.1038/s41419-021-04329-9. PMid: 34741044.
[12] Ke ZB, You Q, Sun JB, et al. A novel ferroptosis-based molecular signature associated with biochemical recurrence-free survival and tumor immune microenvironment of prostate cancer. Front Cell Dev Biol 2021;9:774625. https://doi.org/10.3389/fcell.2021.774625. PMid: 35071228.
[13] Savola S, Klami A, Myllykangas S, et al. High expression of complement Component 5 (C5) at tumor site associates with superior survival in Ewing's sarcoma family of tumour patients. Int Schol Res Notices 2011;2011:168712. https://doi.org/10.5402/2011/168712. PMid: 22084725.
[14] Svoboda LK, Harris A, Bailey NJ, et al. Overexpression of HOX genes is prevalent in Ewing sarcoma and is associated with altered epigenetic regulation of developmental transcription programs. Epigenetics 2014;9(12):1613–25. https://doi.org/10.4161/15592294.2014.988048. PMid: 25625846.
[15] Yu G, Wang LG, Han Y, et al. clusterProfiler: an R package for comparing biological themes among gene clusters. Omics: J Integr Biol 1 2012;6(5):284–7. https://doi.org/10.1089/omi.2011.0118. PMid: 22455463.
[16] Gaujoux R, Seoighe C. A flexible R package for nonnegative matrix factorization. BMC Bioinf 2010;11:367. https://doi.org/10.1186/1471-2105-11-367. PMid: 20598126.
[17] Schenkel FS, Miller SP, Jamrozik J, et al. Two-step and random regression analyses of weight gain of station-tested beef bulls. J Anim Sci 2002;80(6):1497–507. https://doi.org/10.2527/2002.8061497x. PMid: 12078729.
[18] Yoshihara K, Shahmoradgoli M, Martínez E, et al. Inferring tumour purity and stromal and immune cell admixture from expression data. Nat Commun 2013;4:2612. https://doi.org/10.1038/ncomms3612. PMid: 24113773.
[19] Geeleher P, Cox N, Huang RS. pRRophetic: an R package for prediction of clinical chemotherapeutic response from tumor gene expression levels. PLoS One 2014;9(9): e107468. https://doi.org/10.1371/journal.pone.0107468. PMid: 25229481.
[20] Burdach S, Jürgens H. High-dose chemoradiotherapy (HDC) in the Ewing family of tumors (EFT). Crit Rev Oncol Hematol 2002;41(2):169–89. https://doi.org/10.1016/S1040-8428(01)00154-8. PMid: 11856593.
[21] Grevener K, Haveman LM, Ranft A, et al. Management and outcome of Ewing sarcoma of the head and neck. Pediatr Blood Cancer 2016;63(4):604–10. https://doi.org/10.1002/pbc.25830. PMid: 26702872.
[22] Wang SJ, Li D, Ou Y, et al. Acetylation is crucial for p53-mediated ferroptosis and tumor suppression. Cell Rep 2016;17(2):366–73. https://doi.org/10.1016/j.celrep.2016.09.022. PMid: 27705786.
[23] Zhao R, Li Z, Huang Y, et al. A novel ferroptosis-related gene signature for prognosis prediction in Ewing sarcoma. Anal Cell Pathol 2022;2022:6711629. https://doi.org/10.1155/2022/6711629. PMid: 36050939.
[24] Xiao H, Wang J, Yan W, et al. GLUT1 regulates cell glycolysis and proliferation in prostate cancer. Prostate 2018;78(2):86–94. https://doi.org/10.1002/pros.23448. PMid: 29105798.
[25] Min KW, Kim DH, Son BK, et al. High SLC2A1 expression associated with suppressing CD8 T cells and B cells promoted cancer survival in gastric cancer. PLoS One 2021;16(3):e0245075. https://doi.org/10.1371/journal.pone.0245075. PMid: 33735188.
[26] Guo W, Sun S, Guo L, et al. Elevated SLC2A1 expression correlates with poor prognosis in patients with surgically resected lung adenocarcinoma: a study based on immunohistochemical analysis and bioinformatics. DNA Cell Biol 2020;39(4):631–44. https://doi.org/10.1089/dna.2019.5291. PMid: 32096653.
[27] Bluemel G, Planque M, Madreiter-Sokolowski CT, et al. PCK2 opposes mitochondrial respiration and maintains the redox balance in starved lung cancer cells. Free Radic Biol Med 2021;176:34–45. https://doi.org/10.1016/j.freeradbiomed.2021.09.007. PMid: 34520823.
[28] Ma X, Gao Y, Liu JH, et al. Low expression of PCK2 in breast tumors contributes to better prognosis via inducing senescence of cancer cells. IUBMB Life 2022;74(9):896–907. https://doi.org/10.1002/iub.2651. PMid: 35580079.
[29] Chao CH, Wang CY, Wang CH, et al. Mutant p53 attenuates oxidative phosphorylation and facilitates cancer stemness through downregulating miR-200c-PCK2 axis in basal-like breast cancer. Mol Cancer Res 2021;19(11):1900–16. https://doi.org/10.1158/1541-7786.MCR-21-0098. PMid: 34312289.
[30] Goebel G, Berger R, Strasak AM, et al. Elevated mRNA expression of CHAC1 splicing variants is associated with poor outcome for breast and ovarian cancer patients. Br J Cancer 2012;106(1):189–98. https://doi.org/10.1038/bjc.2011.510. PMid: 22108517.
[31] Chen MS, Wang SF, Hsu CY, et al. CHAC1 degradation of glutathione enhances cystine-starvation-induced necroptosis and ferroptosis in human triple negative breast cancer cells via the GCN2-eIF2α-ATF4 pathway. Oncotarget 2017;8(70):114588–602. https://doi.org/10.18632/oncotarget.23055. PMid: 29383104.
[32] Yuan L, Zhang X, Cheng K, et al. IRF1 inhibits autophagy-mediated proliferation of colorectal cancer via targeting ATG13. Cancer Invest 2022;40(1):35–45. https://doi.org/10.1080/07357907.2021.1961265. PMid: 34313498.
[33] Niu Q, Zhao W, Wang J, et al. LicA induces autophagy through ULK1/Atg13 and ROS pathway in human hepatocellular carcinoma cells. Int J Mol Med 2018;41(5):2601–8. https://doi.org/10.3892/ijmm.2018.3499.
[34] Jones RG, Plas DR, Kubek S, et al. AMP-activated protein kinase induces a p53-dependent metabolic checkpoint. Mol Cell 2005;18(3):283–93. https://doi.org/10.1016/j.molcel.2005.03.027. PMid: 15866171.
[35] Das B, Neilsen BK, Fisher KW, et al. A Functional Signature Ontology (FUSION) screen detects an AMPK inhibitor with selective toxicity toward human colon tumor cells. Sci Rep 2018;8:3770. https://doi.org/10.1038/s41598-018-22090-6. PMid: 29491475.
[36] Kopsiaftis S, Sullivan KL, Garg I, et al. AMPKα2 regulates bladder cancer growth through SKP2-mediated degradation of p27. Mol Cancer Res 2016;14

(12):1182–94. https://doi.org/10.1158/1541-7786.MCR-16-0111. PMid: 27638620.
[37] Liu J, Yang M, Kang R, et al. Autophagic degradation of the circadian clock regulator promotes ferroptosis. Autophagy 2019;15(11):2033–5. https://doi.org/10.1080/15548627.2019.1659623. PMid: 31441366.
[38] Yeh CM, Shay J, Zeng TC, et al. Epigenetic silencing of ARNTL, a circadian gene and potential tumor suppressor in ovarian cancer. Int J Oncol 2014;45(5):2101–7. https://doi.org/10.3892/ijo.2014.2627. PMid: 25175925.
[39] Zhang S, Yang Y, Huang S, et al. SIRT1 inhibits gastric cancer proliferation and metastasis via STAT3/MMP-13 signaling. J Cell Physiol 2019;234 (9):15395–406. https://doi.org/10.1002/jcp.28186. PMid: 30710340.
[40] Chen J, Cao L, Li Z, et al. SIRT1 promotes GLUT1 expression and bladder cancer progression via regulation of glucose uptake. Hum Cell 2019;32(2):193–201. https://doi.org/10.1007/s13577-019-00237-5. PMid: 30868406.
[41] Chen DS, Mellman I. Elements of cancer immunity and the cancer-immune set point. Nature 2017;541(7637):321–30. https://doi.org/10.1038/nature21349. PMid: 28102259.